PAPER

Pulsed laser-induced dewetting for the production of noble-metal high-entropy-alloy nanoparticles†

Sye Ghebretnsae, [ID] [a] Tyler Joe Ziehl,[b] Sarah Purdy,[c] Peng Zhang, [ID] [b] Tsun-Kong Sham[d] and Yujun Shi [ID] *[a]

We report the production of quinary AgCuPdPtAu high-entropy-alloy (HEA) nanoparticles using the pulsed laser-induced dewetting (PLiD) technique, which is shown to be a facile approach applicable to both low- and high-melting-point metals. In addition, the atomic composition in the HEA nanoparticles can be controlled by varying the thickness of composite metal in the multi-layer thin films prior to dewetting. The instantaneous heating from the interaction of nanosecond laser pulse with metal and the ultra-fast cooling rate involved in the PLiD process has uniquely positioned it as a non-equilibrium approach to facilitating the formation of HEA nanoparticles with the uniform atomic mixing of different metal elements. We studied the electronic structure and the charge redistribution in the produced AgCuPdPtAu HEA NPs by X-ray photoelectron spectroscopy (XPS) and X-ray absorption near edge structure (XANES). The XPS valence band spectra with significant narrowing in the overall d band and the centroid further away from the Fermi level provide strong evidence for the d-orbital mixing and randomization of different metal components in the HEA nanoparticles. The d-charge redistributions among the constituent metal atoms of Ag, Cu, Pd, Pt, and Au have been further investigated using the XPS core-level spectra and XANES spectra of the five metals. The demonstrated viability of PLiD for the fabrication of HEA NPs and the results on the electronic structure and charge redistribution in the HEA NPs revealed by XPS/XANES would open up many opportunities for the future study of HEA NPs by X-ray spectroscopic techniques.

1. Introduction

High-entropy alloys (HEAs), composed of 5 or more principal elements with near-equal atomic compositions, are a novel alloy design concept first introduced in 2004.[1,2] HEAs enable the incorporation of multiple immiscible elements into a homogenously mixed solid solution driven by the entropy-induced stabilization. They have since become a burgeoning research area attracting enormous interest.[3,4] Compared to the traditional binary and ternary alloys, multi-component HEA metal nanoparticles (NPs) possess a huge space for composition and configuration tunability, providing diverse surface sites for enhancing the activity and selectivity in catalysis.[5] This accordingly provides an excellent platform for new

material discovery and advanced applications in catalysis.[6] Recently, quinary HEA NPs have been demonstrated to serve as highly efficient catalysts in thermo-catalytic reactions such as ammonia oxidation[7] and ammonia decomposition.[8] HEA NPs have also shown superior performances catalyzing a wide range of electrochemical reactions including CO_2 reduction,[9] nitrogen reduction,[10] hydrogen evolution,[11] and alcohol oxidation reactions.[12] To make full use of the power that multi-elemental HEA NPs bring for catalysis, successful synthesis of these NPs that have control over their composition is necessary.

HEA NPs can be synthesized using multiple methods.[13,14] Wet chemical synthesis methods involving the concurrent reduction of all metal salt precursors in colloidal solutions[15,16] have been used to obtain HEA NPs at relatively low temperatures of ~200–250 °C. This technique requires the use of capping and stabilizing agents to have control over the size of the NPs and to prevent their agglomeration. Most other approaches rely on non-equilibrium processes to achieve uniform atomic mixing of different metal elements for the formation of single-phase solid-solution HEA NPs. To this end, Yao *et al.* reported the pioneering carbothermal shock synthesis of HEA NPs consisting of up to eight dissimilar metal elements,[7] where they used a two-step flash heating and

[a]Department of Chemistry, University of Calgary, Calgary, Alberta T2N 1N4, Canada. E-mail: shiy@ucalgray.ca; Tel: +1-403-2108674
[b]Department of Chemistry, Dalhousie University, Halifax, Nova Scotia B3H 4R2, Canada
[c]Saskatchewan Structural Sciences Centre, University of Saskatchewan, Saskatoon, Saskatchewan S7N 5C9, Canada
[d]Department of Chemistry, Western University, London, Ontario N6A 3K7, Canada
†Electronic supplementary information (ESI) available. See DOI: https://doi.org/10.1039/d5nr00988j

cooling of metal precursors on the carbon nanofiber support. The rapid heating at a rate of 10^5 K s^{-1} promoted the atomic mixing of various metals, and the subsequent ultrafast cooling at the same rate allowed for the kinetic trapping of metal atoms in the as-formed single-phase crystalline lattice. The success of the carbothermal shock method has stimulated the development of similar non-equilibrium approaches, such as the ultrasonication-assisted wet chemical synthesis,[17] aerosol-droplet mediated synthesis,[18] fast moving bed pyrolysis,[11] and wireless microwave heating.[19] All the above non-equilibrium approaches involve the conversion of the mixed metal salt precursors to multi-element HEA NPs by co-reduction or pyrolysis *via* fast heating and cooling. Most of the mixed metal salt precursors are in the solution phase, making it challenging to selectively heat the metal ions without the interference of solvent heating.[13] In addition, special requirements for the support substrate may exist in some of the approaches, for example, the presence of functional groups for the absorbance of specific electromagnetic radiation. Hence, more efforts are needed to explore other methods for the synthesis of HEA NPs.

The nanosecond pulsed laser can deliver high energy within an ultra-short duration, it is therefore well suited for providing the fast heating and cooling. Recently, Jiang *et al.* reported the method of laser-induced thermionic emission reduction (LITER) of metal salt precursors under ambient conditions to produce HEA NPs on carbonaceous support.[20] In LITER, free electrons released from the laser-induced thermionic emission in graphene support acted as the reducing agent for an ultrafast reduction of metal ions followed by rapid cooling to form HEA NPs. Rawat *et al.* used the pulsed laser ablation in liquid (PLAL) method for the formation of AlCrCuFeNi NPs, where they found that PLA in deionized water produced phase-segregated core–shell NPs, whereas solid-solution HEA NPs were formed *via* PLA in ethanol.[21] Another method assisted by a pulsed laser to make metallic NPs is known as pulsed laser-induced dewetting (PLiD) of thin metallic films.[22,23] PLiD is a liquid-state dewetting process where thin metallic films undergo morphological changes and break into NPs upon the rapid heating of the metal to its melting point caused by the incident nanosecond laser pulses, followed by ultra-fast cooling for re-solidification.[23,24] The morphological changes in thin metallic films, leading to the formation of NPs, are driven by the tendency to reduce the free energy of the film-substrate-ambient system.[25] The method of PLiD, with its fast processing speed and applicability for a wide variety of metals (including both low- and high-melting-point metals) and substrates, has become a powerful and versatile method for the production of monometallic (*e.g.*, Au,[26] Ag,[27] Cu,[28] Pt,[29] Co,[23] and Ni[30]) and bimetallic (*e.g.*, Au–Ag,[31] Au–Pt,[32] Ag–Co,[33] Pt–Co,[34] and Cu–Ni[35]) NPs with monodisperse size distribution and long-range order.

The instantaneous heating due to the interaction of the nanosecond laser pulse with metal and the ultrafast cooling rate (up to 10^{11} K s^{-1})[22] involved in PLiD makes it comparable to the above-mentioned non-equilibrium approaches, allowing for the kinetic entrapment of the as-formed alloy lattice. It is

therefore uniquely positioned for its potential use in producing atomically mixed HEA NPs. In this work, PLiD was explored to synthesize multi-element metallic NPs composed of Au, Ag, Pt, Pd, and Cu from the multi-layer thin films of the five metals on Si substrates. The specific atomic combination of the five metals in this work serves as a proof-of-principle system to test the applicability of PLiD for the production of noble-metal HEA NPs. PLiD involves fast melting and re-solidification of metals to form metal NPs, where no chemical reactions occur. Therefore, it circumvents the need for metal salt precursors and reducing agents, with the dewetting occurring on multi-layer metallic films. Various parameters critical to the PLiD process, such as the laser fluence and the thickness of the initial multi-layer thin films, were tested. The morphology of the produced NPs was investigated by the field emission scanning electron microscopy (FESEM), and the crystal structure was studied by the high-resolution transmission electron microscopy (HRTEM). Energy dispersive X-ray (EDX) spectroscopy, X-ray photoelectron spectroscopy (XPS), and X-ray absorption spectroscopy (XAS) were used to shed light on the atomic configuration of the metal components and the electronic structures in the produced NPs, which demonstrated the formation of the quinary AgCuPdPtAu HEA NPs.

2. Experimental methods

Si (100) wafers (n-type, phosphorous-doped) with a thickness of 525 ± 25 μm and a resistivity of 1–20 Ω cm (Wafer World Inc.) were cut to sizes of 15 mm × 5 mm and used as substrates for the coating of multi-layer metallic films. Previous investigation of these substrates has demonstrated the presence of a native layer of SiO_2 with 3 nm in thickness on the wafer surface.[24,36] Prior to sputter coating, the Si substrates were first cleaned through sequential rinsing of acetone (ACS reagent grade, ≥99.5%, Sigma-Aldrich), ethanol (absolute, >99.8%, Sigma-Aldrich), and methanol (anhydrous, 99.8%, Sigma-Aldrich), followed by drying under a stream of high-purity N_2 gas (99.999% Praxair). All chemicals were used as received.

The multi-layer metallic films of Ag, Cu, Pd, Pt, and Au were prepared by sequentially sputtering each metal layer with varying thicknesses (1.4–3.7 nm) on the Si substrates using an SCD 500 sputter deposition system (BAL-TEC) under a high-purity argon (99.998%, Praxair) atmosphere at a current of 41 mA and a pressure of 10 mTorr. The thickness of each metal layer was determined by an internal QSG 100 quartz crystal film thickness monitor (BAL-TEC). High-purity metal targets of Ag (99.99%), Cu (99.99%), Pd (99.95%), Pt (99.99%), and Au (99.99%) used in the sputtering were all obtained from the Refining Systems Inc. The three as-sputtered multi-layer thin film samples investigated in this work were Ag(1.6 nm)Cu (1.5 nm)Pd(1.4 nm)Pt(1.5 nm)Au(1.6 nm), Ag(1.6 nm)Cu (1.6 nm)Pd(1.5 nm)Pt(2.7 nm)Au(1.5 nm), and Ag(1.6 nm)Cu (1.6 nm)Pd(1.5 nm)Pt(3.7 nm)Au(1.5 nm). The above sample names have the order of metal indicating the sputtering order and the thickness of each layer represented in the bracket after

the element symbol. It can be seen that the thickness of Pt in the three samples was varied from 1.5 nm, 2.7 nm, to 3.7 nm, and the thicknesses of all other four metal components were kept at ~1.5 nm. The atomic concentrations (in percentage) of each metal in the three as-sputtered thin films were calculated to be $Ag_{18}Cu_{25}Pd_{19}Pt_{19}Au_{19}$, $Ag_{16}Cu_{23}Pd_{17}Pt_{30}Au_{15}$, and $Ag_{14}Cu_{20}Pd_{15}Pt_{37}Au_{13}$, respectively. Considering that only the Pt film thickness was significantly varied, leading to the difference in the Pt atomic composition, in the three as-sputtered films, we have adopted a short label indicating only the Pt atomic percentage for the three samples as MM-Pt$_{19}$, MM-Pt$_{30}$, and MM-Pt$_{37}$, respectively, where MM represents multi-metallic.

PLiD of the as-sputtered multi-layer metallic thin films was carried out in ambient by irradiating the samples with the 355 nm UV output from a Q-switched Nd:YAG laser (Spectra-Physics, LAB-170-10). The 355 nm laser irradiation has a pulse width of 9 ns and a repetition rate of 10 Hz. Various laser fluences ranging from 25 mJ cm^{-2} to 500 mJ cm^{-2} were investigated in this work to explore its effect on the morphology evolution of the thin films, from which the threshold fluence for full dewetting was determined. These laser fluences are well below the ablation threshold fluence for the five constituent metals to ensure that the laser energy only causes the heating of metals, rather than the ablation. The morphologies of the samples were examined using a field emission scanning electron microscope (FESEM, Zeiss Sigma VP) under ultra-high vacuum (<10^{-10} Torr) at an accelerating voltage of 10 kV. FESEM images were analysed using the software ImageJ to determine the size and the size distribution of the NPs. EDX spectroscopic analysis was performed on the multi-metallic NPs to determine their elemental composition and to obtain elemental mapping, using an INCA x-act EDX instrument (Oxford Instruments). The crystal structure of the produced multi-metallic NPs was investigated using high-resolution transmission electron microscope (HRTEM). For this, the AgCuPdPtAu NPs produced from PLiD of multi-layer thin films were removed from the Si substrates into colloidal solution, following a procedure as described in our previous work.[36] They were then drop-cast onto the TEM grid (Lacey carbon-Ni, Electron Microscopy Sciences) for analysis. The HRTEM was carried out using a Talos F200X G2 S/TEM (Thermo Fisher) operating at an acceleration voltage of 200 kV.

XPS measurements were carried out on as-sputtered thin films composed of Ag, Cu, Pd, Pt, and Au as well as the multi-metallic NPs after PLiD using an AXIS Supra X-ray photoelectron spectrometer (Kratos Analytical). A monochromatic aluminum (Al) K$_\alpha$ source at a photon energy of 1486.6 eV was used, with a spot size of 300 × 700 μm, a pass energy of 20 eV, and a step size of 0.05 eV, for collecting high-resolution scans. The base pressure of the system was 9 × 10^{-9} Torr. The X-ray source was operated with an accelerating voltage of 15 keV and an emission current of 15 mA. The binding energy values in the valence band spectra were referenced to the Fermi level in the region, and those in the core-level spectra were calibrated to carbon (C) 1s at 284.5 eV. Data fitting was performed in CasaXPS using Shirley baselines and asymmetric line shapes.[37]

The XAS spectra for the Cu, Ag, and Pd K edges, and Pt and Au L$_3$ edges were collected at the Sector 25 beamline at the Advanced Photon Source at Argonne National Laboratory in Lemont, Illinois. Spinners were used to rotate the samples to avoid diffraction peaks from the thick Si–wafer substrate. The spectra were collected in fluorescence mode using a Vortex detector to improve the sensitivity of the measurements due to low concentrations of the metals on the Si–wafer substrate. Bulk metallic foils for the respective elements were measured simultaneously in transmission mode for calibration during data processing and analysis. All samples were measured in ambient conditions. The XAS spectra were normalized using standard procedures.[38]

3. Results and discussion

PLiD, a liquid-state dewetting method, of metallic thin films only occurs when the laser energy density (*i.e.*, fluence) is above the melting threshold of the metal.[22,23] Above the threshold fluence, the processes of rapid melting (in approximately 0.1–1 ps) and subsequent re-solidification (in approximately 10 ps)[23] of metals take place within a single nanosecond laser pulse. It is therefore important to first determine the threshold laser fluence for a successful PLiD process leading to the formation of metal NPs. For this, varied fluence ranging from 25 to 500 mJ cm^{-2} was explored. PLiD was carried out for the as-sputtered MM-Pt$_{19}$ thin film samples at a constant laser irradiation time of 10 s (*i.e.*, 100 pulses). Fig. 1a–j shows the FESEM images of the thin film both prior to and after PLiD at the varying fluences. No dewetting occurs at the two lowest fluences of 25 and 50 mJ cm^{-2}, as indicated by the nearly identical morphology of the sample at 50 mJ cm^{-2} (Fig. 1b) to that of the as-sputtered film (Fig. 1a). At the next higher fluence of 75 mJ cm^{-2} (Fig. 1c), initial film breaking occurs with the formation of holes. Partial dewetting of thin film continues at 100 and 150 mJ cm^{-2} (Fig. 1d and e) with further film breaking, forming some isolated NPs.

Complete dewetting into NPs was observed at 200 mJ cm^{-2} and above (Fig. 1f–j). Therefore, the threshold fluence required for complete PLiD of multi-layer MM-Pt$_{19}$ thin films into isolated NPs, was determined to be between 150 and 200 mJ cm^{-2}. Previous studies of PLiD of single-layer Ag (melting point (m.p.) 1235 K) and Au (m.p. 1337 K) films on Si substrates using the same laser wavelength of 355 nm have reported the threshold fluence of 50–81 mJ cm^{-2} (ref. 27) and 49–75 mJ cm^{-2},[24] respectively, whereas that of the single-layer Pt (m.p. 2041 K) on Si substrates was determined to be 322–400 mJ cm^{-2}.[39] When compared to the threshold fluences of Ag, Au and Pt, it is interesting to note that the value for the multi-layer quinary films of AgCuPdPtAu at 150–200 mJ cm^{-2} is higher than the two with the lowest m.p. (*e.g.*, Ag, Au), but significantly lower than the one for Pt, which is the metal of the highest m.p. among the five. This suggests that less energy
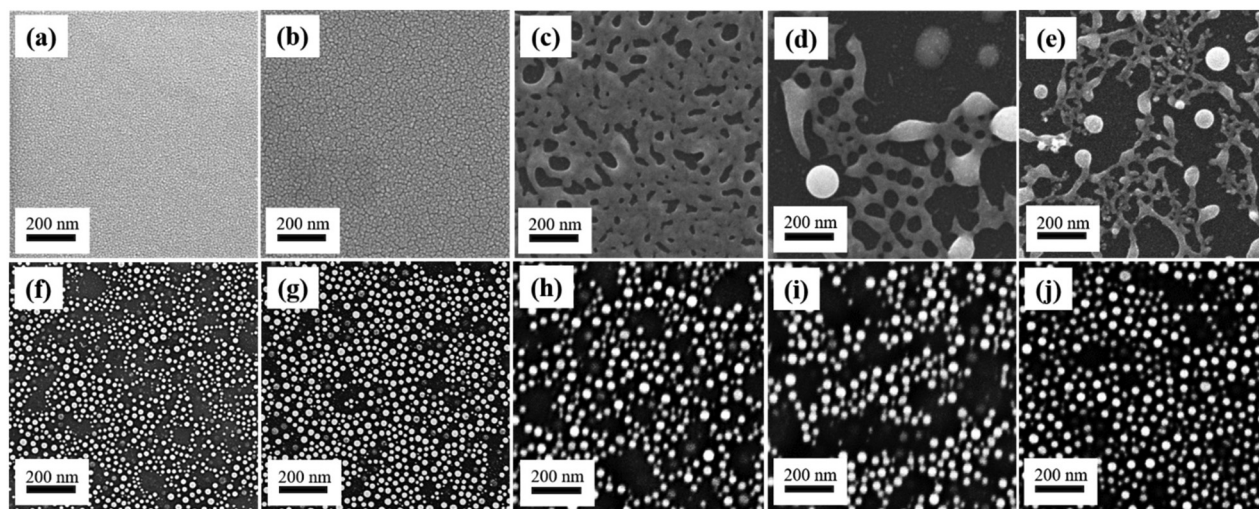
Fig. 1 FESEM images of the (a) the as-sputtered $Ag_{18}Cu_{25}Pd_{19}Pt_{19}Au_{19}$ (MM-Pt_{19}) multilayer thin films, and the MM-Pt_{19} samples after PLiD for 10 s at a laser fluence of (b) 50 mJ cm^{-2}, (c) 75 mJ cm^{-2}, (d) 100 mJ cm^{-2}, (e) 150 mJ cm^{-2}, (f) 200 mJ cm^{-2}, (g) 250 mJ cm^{-2}, (h) 300 mJ cm^{-2}, (i) 400 mJ cm^{-2}, and (j) 500 mJ cm^{-2}.

is required to melt Pt in the presence of four other metal components, likely due to the favorable mixing when there are five metal components. At the varying fluence of 200–500 mJ cm^{-2}, the average metal NP sizes ranged from 21 ± 4 nm to 40 ± 7 nm, showing an initial increase in NP size when the fluence changed from 200 to 300 mJ cm^{-2}, then stayed relatively constant from 300–500 mJ cm^{-2}, as illustrated in the plot of NP size *vs.* the laser fluence in Fig. S1.†

To test whether PLiD can be employed to produce multi-metallic quinary NPs of different atomic composition, three samples of multi-layer AgCuPdPtAu thin films, *i.e.*, MM-Pt_{19}, MM-Pt_{30}, and MM-Pt_{37}, each having a different composition of Pt due to the different Pt film thickness of 1.5 nm, 2.7 nm, and 3.7 nm, respectively, were investigated. The PLiD experiments were performed at a laser fluence of 250 mJ cm^{-2} and

an irradiation time of 10 s. The FESEM images of the three samples after PLiD were shown in Fig. 2, showing the formation of NPs for all three samples by the complete dewetting regardless of the atomic composition. The average NP size for samples MM-Pt_{19}, MM-Pt_{30}, and MM-Pt_{37} were 25 ± 4 nm, 23 ± 4 nm, and 26 ± 5 nm, respectively. The produced NPs showed little variation in their size with increasing Pt thickness in the initial thin film, which is in good agreement with the similar independent relationship between the NP size and initial film thickness in the PLiD of single-layer Pt[39] and Ag[27] films on Si substrates, explained by the fact that the dewetting process follows the mechanism of nucleation and growth of holes.

EDX spectroscopic analysis was performed to investigate if multi-metallic quinary NPs were formed and to determine the elemental composition of the produced metallic NPs from
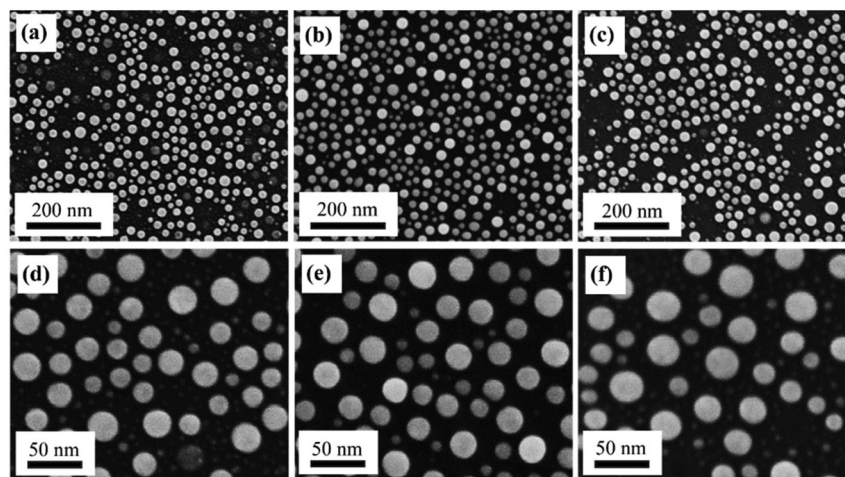
Fig. 2 FESEM images of the metallic NPs produced from PLiD of (a) MM-Pt_{19}, (b) MM-Pt_{30}, and (c) MM-Pt_{37} samples at a laser fluence of 250 mJ cm^{-2} and an irradiation time of 10 s. The high-magnification images corresponding to (a), (b), and (c) are shown in (d), (e), and (f), respectively.
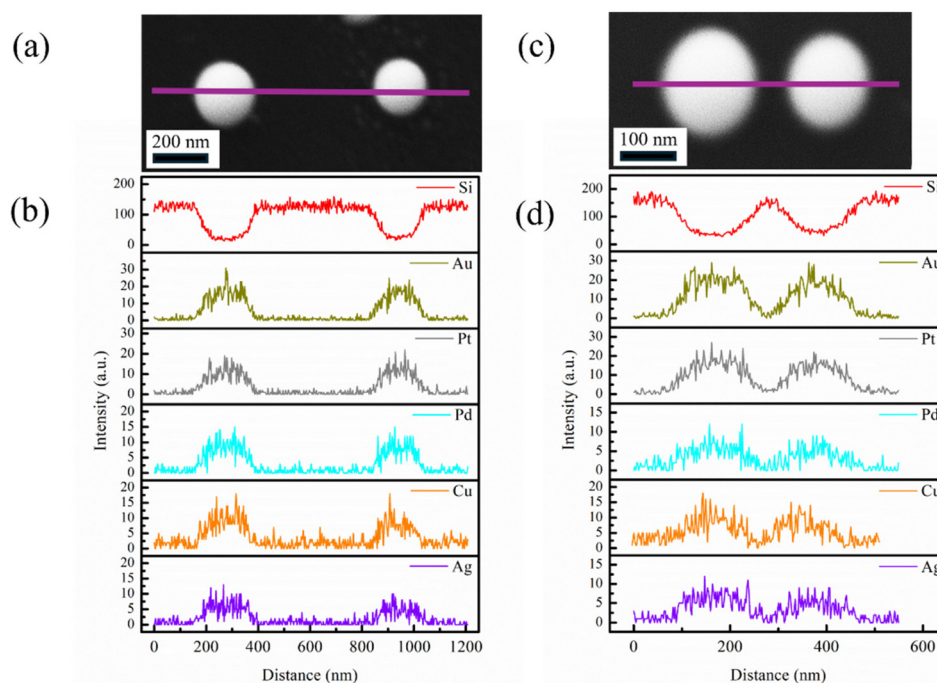
Fig. 3 (a) FESEM image and (b) the corresponding EDX line scan across the NPs for the sample of MM-Pt$_{19}$, and (c) FESEM image and (d) the corresponding EDX line scan across the NPs for the sample of MM-Pt$_{30}$.

PLiD. Fig. 3a–d shows the EDX line scans across NPs produced from PLiD of the two samples of MM-Pt$_{19}$ and MM-Pt$_{30}$ at 250 mJ cm^{-2} for 10 s, along with the corresponding FESEM images. The EDX line scans across the multiple NPs show the presence of all 5 metals of Ag, Cu, Pd, Pt, and Au, coupled with the concurrent reduction of signals from Si, due to the NPs covering the Si substrates. The elemental maps illustrated in Fig. 4 for the same two samples also show the presence of each metal in the NP area, all of which are distributed uniformly, with no observed regions rich in one metal, indicating no phase segregated region in the NPs being formed. The same was observed for MM-Pt$_{37}$ NP samples, whose EDX line scans and elemental maps are shown in Fig. S2 and S3,† respectively.

The EDX analysis was also used to determine the atomic concentration of each metal in the NPs for the three samples, and the results are summarized in Table 1. The corresponding atomic compositions of the as-sputtered thin films are also listed for comparison. The atomic concentrations of Pt in the NPs were observed to increase with its thickness in the initial metal films. This indicates that the technique of PLiD can control the atomic concentration of the multi-metallic NPs by varying the thickness of the sputtered films, which provides a facile way to control the atomic composition using PLiD.

To understand the crystal structure of the produced AgCuPdPtAu NPs, HRTEM analysis was performed. Fig. 5 shows the HRTEM images of the MM-Pt$_{19}$ NPs, with the corresponding lattice spacing show in Fig. 5c. The d-spacing determined from the HRTEM is 2.175 Å. All five constituent metals of Ag, Cu, Pd, Pt, and Au in our HEA NPs have face-centered

cubic (FCC) lattice with the space group of *Fm3m*. By applying the Vegard's law, the predicted lattice constant for the MM-Pt$_{19}$ alloy is 3.8987 Å, and the corresponding d-spacing for the (111) plane is 2.251 Å. Based on this, the d-spacing determined from the HRTEM for the MM-Pt$_{19}$ NPs at 2.175 Å is most likely from the (111) plane of the alloy lattice. This provides strong evidence that the five metals in the MM-Pt$_{19}$ NPs are alloyed, and the NPs are crystalline, possessing the FCC lattice, as expected. The lattice constant for the MM-Pt$_{19}$ NPs is calculated to be 3.767 Å.

The electronic structure of the synthesized quinary HEA NPs was investigated using XPS. Fig. 6 shows the valence band (VB) spectra of all three NP samples of MM-Pt$_{19}$, MM-Pt$_{30}$, and MM-Pt$_{37}$, along with those from the as-sputtered films prior to PLiD for comparison. The VB region in the thin film samples is clearly dominated by the Au and Pt character, as seen in the doublet peaks at 6.5 eV and 4.0 eV corresponding to the Au 5d spin–orbit split bands,[40] and the distinct Femi edge of Pt 5d band,[41] represented by the high intensity in the density of state (DOS) near the Fermi level. This is expected as Au and Pt are the two topmost layers of the sputtered films, which was observed in similar work.[32] It is also noted that the Fermi edge relative to the d band maximum is higher with increasing Pt content underneath the top Au layer. In the AgCuPdPtAu HEA NP samples after PLiD, the DOS intensity at the Fermi level drops significantly and the Au 5d splitting is lost. This decrease in the Pt and Au character suggests that both Au and Pt are diluted, forming alloys.[40] The overall d band also narrows significantly and moves away from the Fermi level, indicating that randomization of different metal components
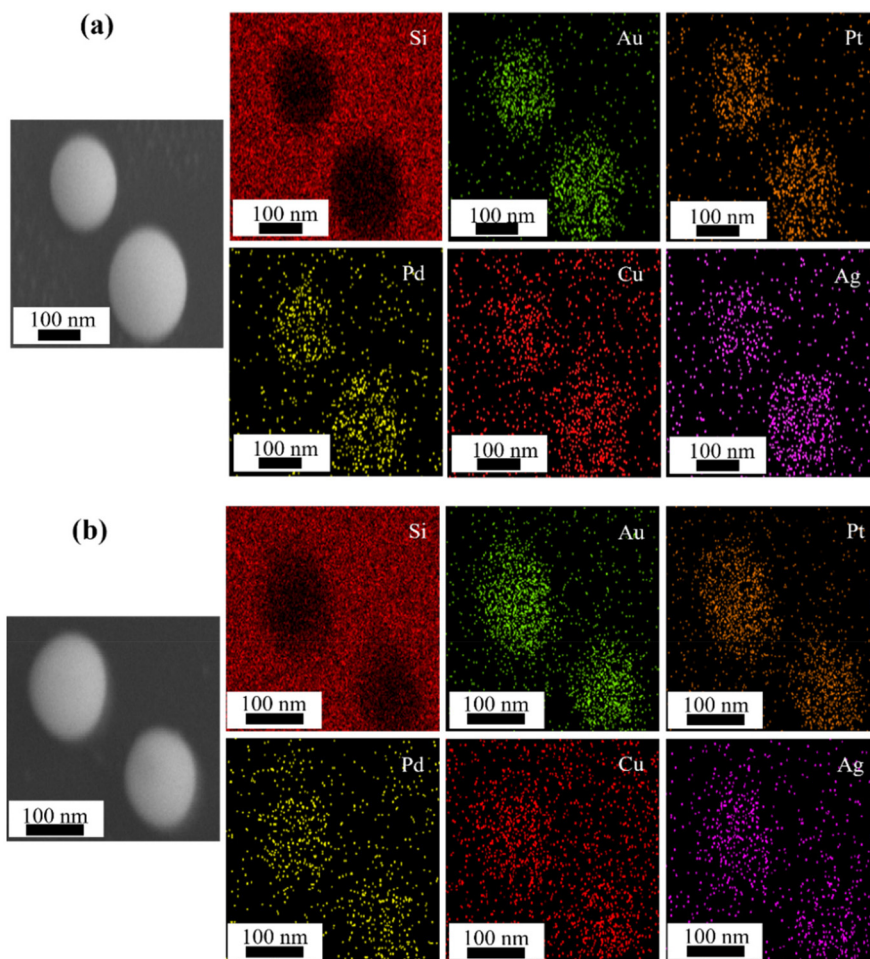
Fig. 4 FESEM images of quinary AgCuPdPtAu NPs and corresponding EDX elemental maps of (a) MM-Pt$_{19}$ and (b) MM-Pt$_{30}$ NPs *via* PLiD at 250 mJ cm^{-2} and 10 s.

Table 1 Atomic concentrations (in percentage) of the AgCuPdPtAu NP samples for MM-Pt$_{19}$, MM-Pt$_{30}$, and MM-Pt$_{37}$ from the EDX analysis as compared to those of the initial thin films

Sample	Ag	Cu	Pd	Pt	Au
MM-Pt$_{19}$ thin film	18 ± 1	25 ± 1	19 ± 1	19 ± 1	19 ± 1
MM-Pt$_{19}$ NPs	13 ± 2	33 ± 3	24 ± 2	17 ± 2	13 ± 2
MM-Pt$_{30}$ thin film	16 ± 1	23 ± 1	17 ± 1	30 ± 1	15 ± 1
MM-Pt$_{30}$ NPs	15 ± 2	26 ± 3	19 ± 2	28 ± 2	12 ± 2
MM-Pt$_{37}$ thin film	14 ± 1	20 ± 1	15 ± 1	37 ± 1	13 ± 1
MM-Pt$_{37}$ NPs	13 ± 2	20 ± 2	16 ± 2	41 ± 2	11 ± 2

most likely occur upon laser irradiation, leading to alloying in the produced NPs.[42,43] Furthermore, the VB spectra of AgCuPdPtAu HEA NPs appear to show no clear peaks from the individual metal constituents. For example, the characteristic spin–orbit splitting of the Au–Au interaction in Au 5d band disappears and the sharp VB edge at the Fermi level from the strong Pt–Pt interaction diminishes. Wu *et al.* have demonstrated in their work that the featureless VB spectra is a characteristic feature for HEA NPs caused by the hybridization of

d-orbitals between different elements.[44,45] Hence, the observed featureless VB spectra for our HEA NP samples provide a further strong support for the feasibility of PLiD in producing HEA NPs. There is little variance in the VB spectra for all three HEA NP samples, indicating that the method of PLiD can fully disperse the different metals regardless of the Pt concentration.

High-resolution XPS spectra of the core-level regions of the composite metals were investigated to provide further insight into the charge redistribution following PLiD. The Au 4f and Pt 4f XPS spectra of the multi-layer thin films are shown in Fig. S4a and S4b,† respectively, with the fitting component binding energies (BEs) presented in Table S1.† The Pt and Au in the multi-layer thin film samples prior to PLiD are essentially pure Au and Pt, giving the two Au^0 4f doublet peaks at 84.0–84.1 eV (4f$_{7/2}$) and 87.6–87.8 eV (4f$_{5/2}$) and the two Pt^0 4f peaks at 71.0–71.1 eV (4f$_{7/2}$) and 74.4–74.5 eV (4f$_{5/2}$). The XPS spectra of the AgCuPdPtAu HEA NPs achieved after PLiD are shown in Fig. 7. In the Au 4f regions (Fig. 7a), the metallic Au^0 peaks were observed; however, an additional doublet with higher BE was observed with appreciable intensities at
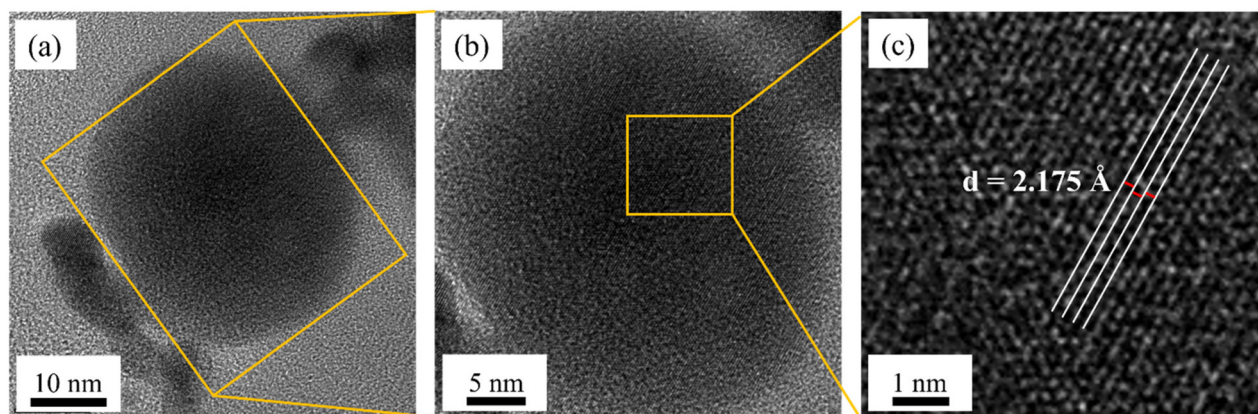
Fig. 5 (a and b) HRTEM images with (c) the corresponding lattice spacing on the HEA NP of MM-Pt$_{19}$ on the TEM grid after removal from the substrate. The MM-Pt$_{19}$ NPs were produced from PLiD at 300 mJ cm^{-2} and 20 s.
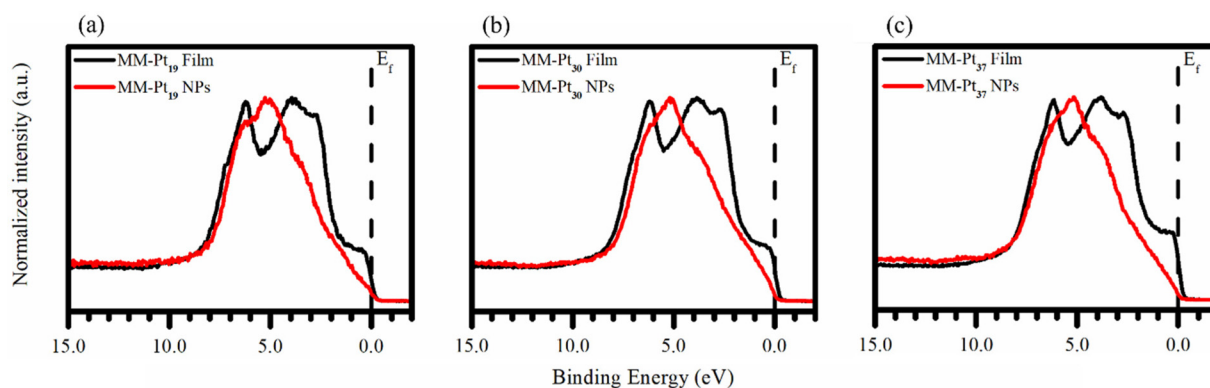
Fig. 6 Normalized XPS valence band spectra of the three samples of (a) MM-Pt$_{19}$, (b) MM-Pt$_{30}$, and (c) MM-Pt$_{37}$ for both as-sputtered thin films prior to dewetting (black) and HEA NPs (red) after PLiD at 250 mJ cm^{-2} and 10 s.

85.0–85.2 eV (Au$^{\delta+}$ 4f$_{7/2}$) and 88.7–88.8 eV (Au$^{\delta+}$ 4f$_{5/2}$). The shift in BE (+1.0–1.2 eV) is lower than what would be expected for Au$_2$O/AuO (+1.4–1.5 eV) and Au$_2$O$_3$ (+1.8–2.1 eV) NPs.[46] This relatively small BE shift in the Au$^{\delta+}$ 4f peaks suggests that it is not from the Au oxides, but rather indicates the presence of slightly positively charged Au$^{\delta+}$ species in the HEA NPs, which is in good agreement with the charge compensation behavior at the Au site upon alloying.[40,47,48] According to the charge compensation model, Au loses d electrons, but the d-charge depletion is overcompensated by a gain of the s-like conduction electrons. This effect has been observed in many Au binary alloys.[40,47,48] The loss of d electrons in Au leads to a positive 4f BE shift due to the higher coulombic potential caused by the larger screening effect from the d electrons. Therefore, the presence of the positive charged Au$^{\delta+}$ species suggests the alloying of Au with other metal atoms in the HEA NPs.

The Pt 4f region represented in Fig. 7b showed that the HEA NP surface contained at least two new components with a noticeable positive and a negative shift in BE, respectively, relative to the Pt^0 metal. Specifically, for Pt 4f$_{7/2}$, the two components of Pt$^{\delta+}$ and Pt$^{\delta-}$ appeared at 72.7–72.9 eV and

70.8–70.9 eV, respectively, showing a BE shift relative to Pt^0 of +1.7–1.8 eV and −0.2 eV, respectively. All the BEs for the Au 4f and Pt 4f peaks in the AgCuPdPtAu HEA NPs are listed in Table 2. In their study of the charge redistribution behavior of Pt–Au alloys, Wang et al.[40] reported a negative shift in the BE of Pt 4f core level when forming alloys with Au. In addition, Belkhou et al.[49] showed a shift of the Pt 4f$_{7/2}$ to a lower BE (i.e., 70.64–70.75 eV) when it formed an alloy with Cu. Therefore, the Pt$^{\delta-}$ component is mostly likely from the Pt–Au interaction with also the contribution from the presence of Pt–Cu alloy in the AgCuPdPtAu HEA NPs. The Pt oxide species are expected to have BE shifts of +1.3 eV (PtO) and +3.0 eV (PtO$_2$),[50] indicating that the Pt$^{\delta+}$ component is not likely to be assigned to Pt oxides. Hence, this component suggests the presence of some electron-deficient Pt species from the randomization of Pt in the HEA NPs. A third component, Pt$^{\Delta+}$, was observed for 4f$_{7/2}$ at 71.7 eV and 4f$_{5/2}$ at 75.0 eV only in the MM-Pt$_{37}$ sample with the highest Pt concentration.

Additionally, in this spectral region for Pt 4f, the Cu 3p contribution (3p$_{3/2}$ at 75.5 eV and 3p$_{1/2}$ at 77.5 eV), absent in the thin film samples prior to PLiD, can be seen in the two NP
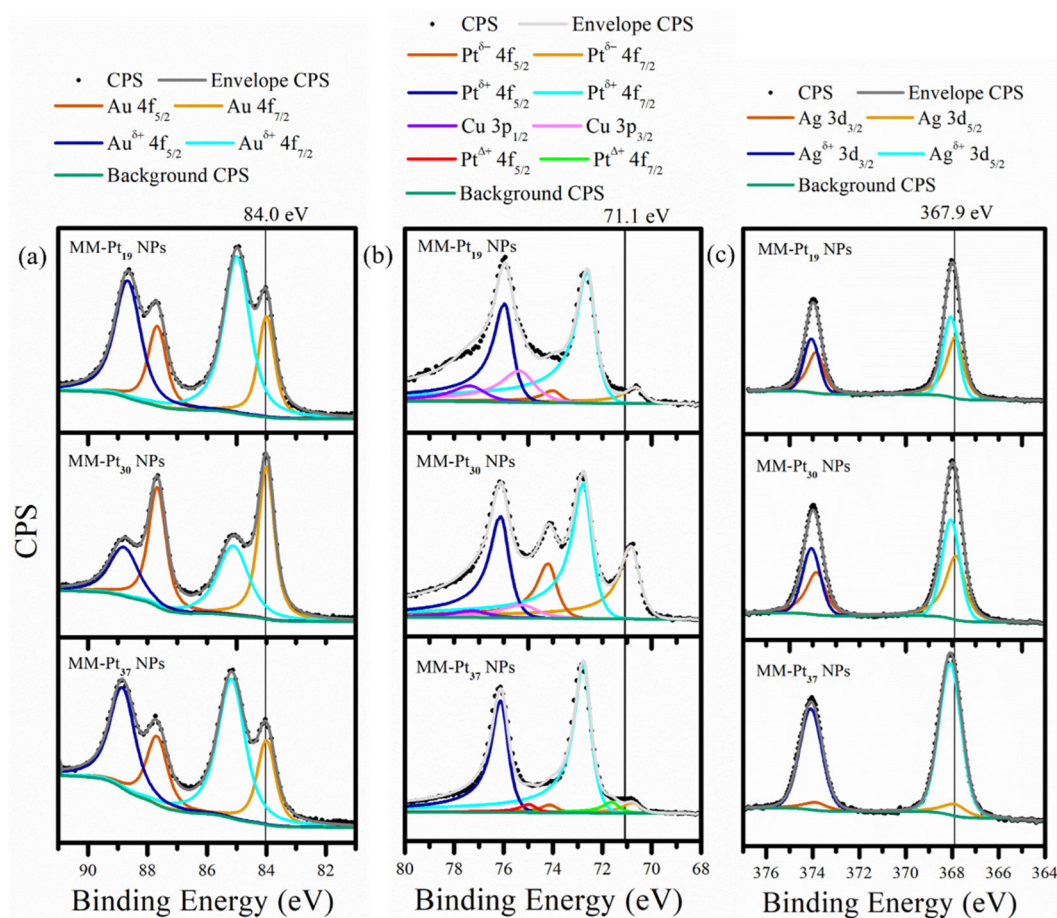
The XPS spectra of Ag 3d in the as-sputtered multi-layer films shown in Fig. S4c† yielded the metallic Ag^0 peaks of $3d_{5/2}$ at 367.8–367.9 eV and $3d_{3/2}$ at 373.8–373.9 eV. After PLiD, as shown in Fig. 7c and Table 2, the NP samples showed the two Ag^0 3d peaks and a second pair of $Ag^{\delta+}$ 3d peaks at higher BE of 368.1 eV (ΔBE = +0.2–0.3 eV) and 374.1 eV (ΔBE = +0.2–0.3 eV). Previous studies on the charge redistribution in Au–Ag[47] and Pd–Ag[51] binary alloys have shown that Ag gains 4d charge and loses non-d charge (*i.e.*, s–p conduction electrons) upon alloying, leading to a negative shift in Ag 3d core-level BE. The observed $Ag^{\delta+}$ species in the HEA NPs may indicate that Ag also interacts with metal atoms other than Au and Pd, *e.g.*, Pt and Cu, in the NPs.

Fig. 8 shows the high-resolution XPS spectra in the Pd 3d region for both the as-sputtered thin film and HEA NP samples after PLiD for MM-Pt$_{19}$, MM-Pt$_{30}$, and MM-Pt$_{37}$. In the thin film samples, the Au $4d_{5/2}$ (at 335.2 eV) contribution dominates this region as it is the topmost layer. The Pt $4d_{5/2}$ (at 330.5 eV) from the second topmost layer was also present. The Pd 3d peaks are from the metallic Pd^0 at 335.4–335.7 eV ($3d_{5/2}$) and 340.7–340.9 eV ($3d_{3/2}$). XPS spectra of HEA NP samples in this region showed very different features from those in the thin films. The Au 4d contribution is no longer dominant in the NPs but is replaced by multiple Pd components in this region. This confirms the randomization of Au atoms derived from the analysis of the VB spectra. Among the Pd components, the two stronger ones are the metallic Pd^0 observed at $3d_{5/2}$ 335.4–335.6 eV and the $Pd^{\delta+}$ component at higher BE at $3d_{5/2}$ 337.0–337.2 eV. A relatively weak component is from $Pd^{\delta++}$ at even higher BE at $3d_{5/2}$ 338.7 eV. This further shows the mixing of metals upon laser dewetting. The BEs for all the Pd 3d peaks in the AgCuPdPtAu HEA NPs are listed in Table 3. In a previous study for the bimetallic Pd–Pt alloy NP system by Li *et al.*,[52] where d-charge redistribution occurs from Pt to Pd, the Pd 3d peaks showed a splitting into Pd^0 and $Pd^{\delta+}$, indicative of an electron-rich environment. Hence, the presence of multiple Pd components in the Pd 3d region suggests also a flow of electrons to Pd from other metallic sites such as Au and Pt in the NPs, as will be further discussed in the analysis of X-ray absorption spectra.

The high-resolution Cu $2p_{3/2}$ XPS spectra collected for both the thin films and HEA NPs *via* PLiD for the three samples of MM-Pt$_{19}$, MM-Pt$_{30}$, and MM-Pt$_{37}$ are shown in Fig. 9 and Table 3. Similarly, the thin film samples show dominantly
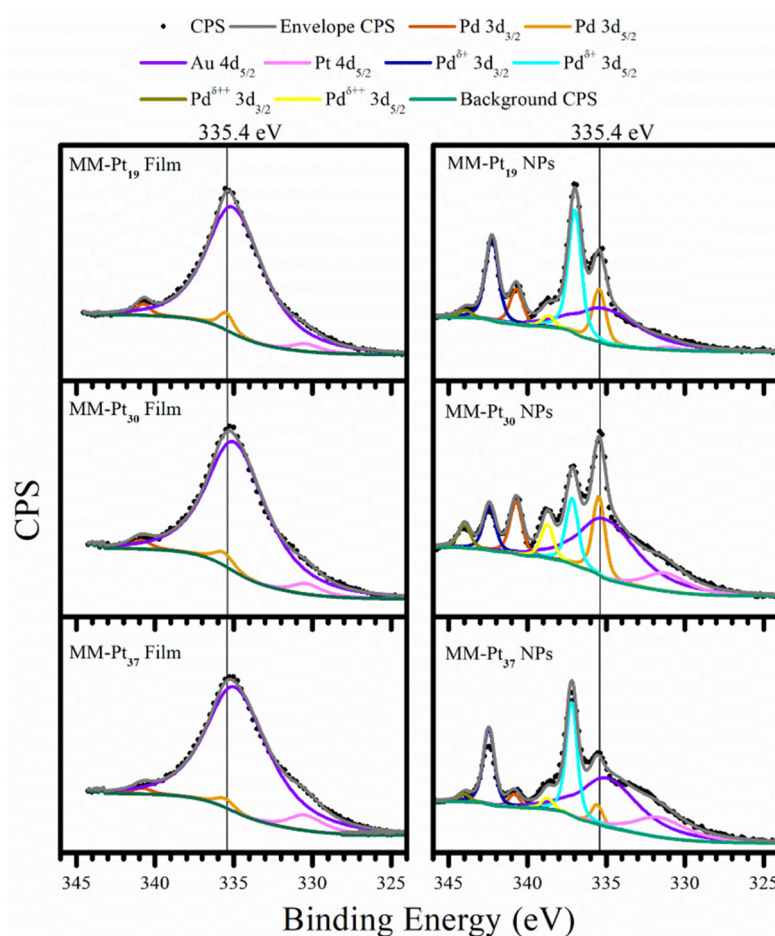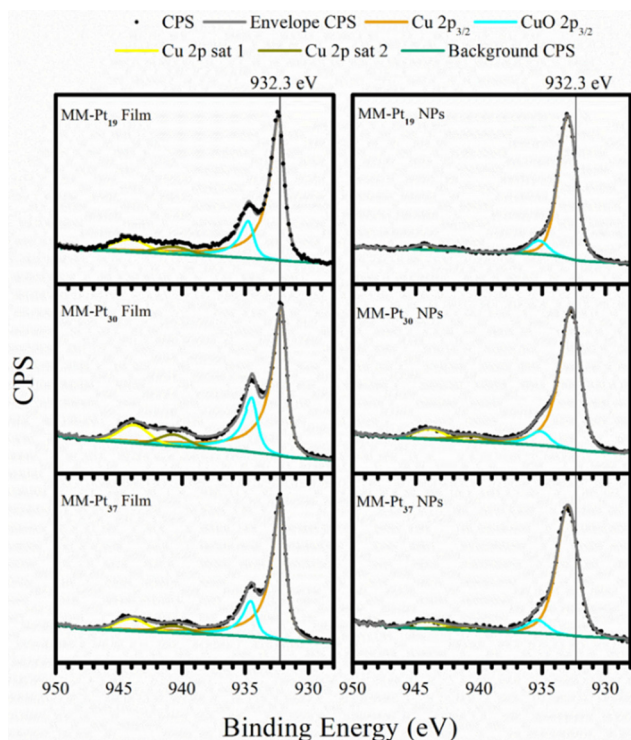

Fig. 8 XPS spectra and peak fit in the Pd 3d region for the AgCuPdPtAu HEA NP samples of MM-Pt$_{19}$, MM-Pt$_{30}$, and MM-Pt$_{37}$.

Table 3 Binding energies of Pd 3d and Cu $2p_{3/2}$ peaks and peak widths (FWHM) from the XPS analysis of the AgCuPdPtAu HEA nanoparticle samples of MM-Pt$_{19}$, MM-Pt$_{30}$, and MM-Pt$_{37}$

Pd 3d	Pd $3d_{5/2}$ (eV)	FWHM (eV)	Pd $3d_{3/2}$ (eV)	FWHM (eV)	$Pd^{\delta+}$ $3d_{5/2}$ (eV)	FWHM (eV)	$Pd^{\delta+}$ $3d_{3/2}$ (eV)	FWHM (eV)	$Pd^{\delta++}$ $3d_{5/2}$ (eV)	FWHM (eV)	$Pd^{\delta++}$ $3d_{3/2}$ (eV)	FWHM (eV)
MM-Pt$_{19}$	335.4	1.0	340.7	1.0	337.0	1.0	342.3	1.0	338.7	1.0	343.9	1.0
MM-Pt$_{30}$	335.5	1.0	340.7	1.0	337.2	1.0	342.4	1.0	338.7	1.0	344.0	1.0
MM-Pt$_{37}$	335.6	0.9	340.8	0.9	337.2	0.9	342.5	0.9	338.7	0.9	344.0	0.9

| Cu $2p_{3/2}$	$Cu^{\delta+}$ $2p_{3/2}$ (eV)	FWHM (eV)	$CuO^{\delta+}$ $2p_{3/2}$ (eV)	FWHM (eV)
MM-Pt$_{19}$	933.0	1.7	935.2	1.7
MM-Pt$_{30}$	932.6	1.7	935.0	1.7
MM-Pt$_{37}$	932.8	1.9	935.3	1.9

Fig. 9 XPS spectra and peak fit of the AgCuPdPtAu HEA NP samples of MM-Pt$_{19}$, MM-Pt$_{30}$, and MM-Pt$_{37}$ in the Cu 2p region.

metallic Cu^0 peaks at $2p_{3/2}$ 932.2–932.3 eV. However, appreciable contribution from CuO at $2p_{3/2}$ 934.5–934.8 eV (ref. 53) is also present, indicating the oxidation of Cu in the films prior to PLiD. In the NP samples, both peaks have shifted to higher BEs with Cu$^{\delta+}$ $2p_{3/2}$ at 932.6–933.0 eV and (CuO)$^{\delta+}$ $2p_{3/2}$ at 935.0–935.3 eV. In the NP samples, the contribution of the CuO, in the form of (CuO)$^{\delta+}$, however appeared with much reduced relative intensities to those from Cu$^{\delta+}$, indicating that the treatment of the films through PLiD results in the depletion of the Cu oxides in the NPs. This would suggest that the Cu atoms are more stable in the HEA NPs as compared to those in the thin films, yielding more metallic Cu in the HEA NPs.

X-ray absorption spectroscopy (XAS) was pursued to further characterize the electronic properties of the HEA NPs through the examination of the X-ray absorption near edge structure (XANES) of the alloyed NPs at the L$_3$ edge for Au and Pt and the K edge for Ag, Pd, and Cu. Fig. 10 shows the XANES spectra of the HEA NP samples of MM-Pt$_{19}$ for all five metal components along with those from the pure metal foil references. The Au L$_3$-edge XANES spectra (Fig. 10a) show similar near edge features for both the reference foil and the HEA NPs. However, the intensities of the absorption edges, *i.e.*, the white-line intensity, for the two samples vary, with the NPs having a greater intensity compared to the foil. Typically, this change in the absorption intensity would be from an increase in the metal's oxidation state. However, due to the low tendency of Au to be oxidized, and the lack of Au oxide observed in the NPs from the XPS spectra, this increase in intensity is related to the electron donation occurring between the 5d orbitals in Au with other elements as has been observed previously.[47,54–56] This also agrees with the Au 5d depletion upon alloying, following the charge compensation model that has been shown in many Au-containing binary alloys such as Au–Pt[40] and Au–Cu.[47] In the Pt L$_3$-edge XANES spectra (Fig. 10b), the NP sample shows an evidently higher white-line intensity for the L$_3$ edge when compared to the XANES spectra of the reference foil. As with Au, since there was no presence of Pt oxides observed in the XPS spectra, this increase in absorption intensity could be associated with some amount of electron donation occurring from the 5d orbitals of Pt in the NPs. Similar observation in the Pt L$_3$-edge white-line intensity was reported in the Pt–Pd alloy NPs where d-charge redistribution was shown to occur from Pt (d-charge depletion) to Pd (d-charge gain).[52]

The K-edge spectra for Ag, Pd, and Cu were also shown in Fig. 10. The shape of the near edge feature in the Ag K-edge XANES spectra (Fig. 10c) for the HEA NPs is similar to that of the reference foil but is observed to occur at a lower energy for the NP sample. This shift to the lower energy indicates a potential decrease in the Ag oxidation state, suggesting electron gaining into the Ag 4d orbitals. This agrees with the behavior of Ag in both Au–Ag[48] and Pd–Ag[51] alloys that Ag gains d-charge and loses s–p conduction electrons. The Pd K-edge
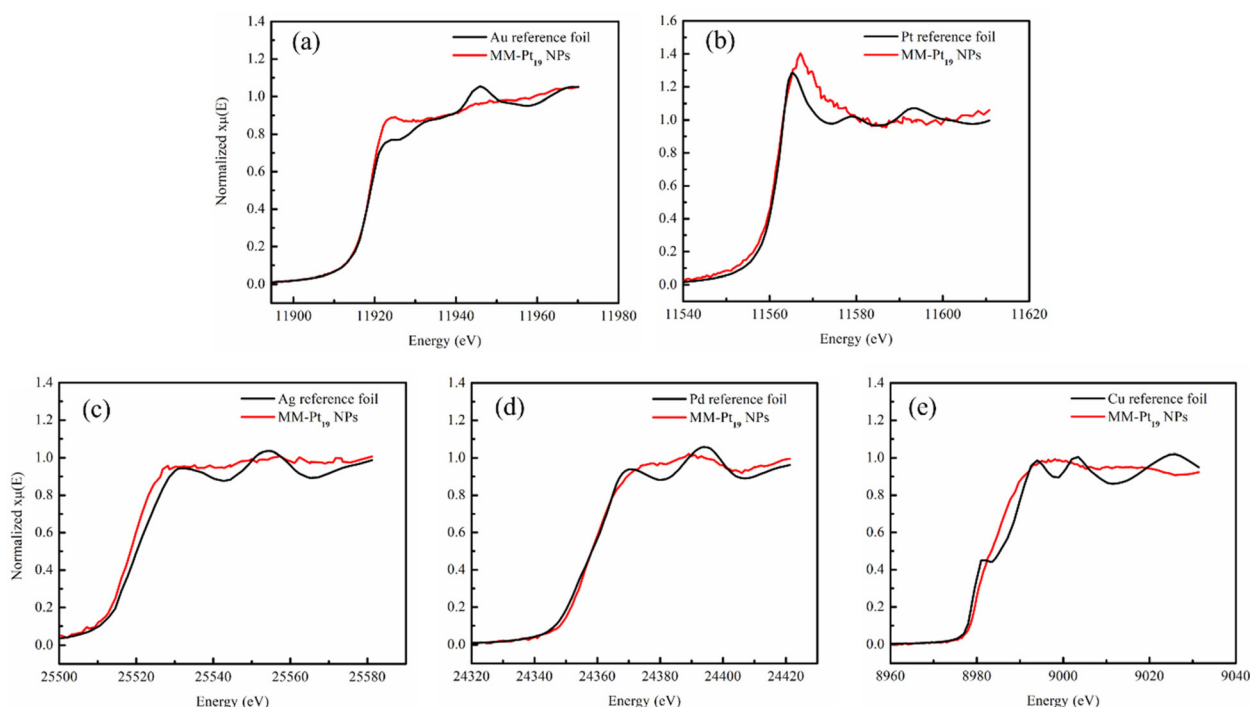
Fig. 10 XANES spectra of the MM-Pt$_{19}$ NP sample for the (a) Au L$_3$ edge, (b) Pt L$_3$ edge, (c) Ag K edge, (d) Pd K edge, and (e) Cu K edge. The spectra from the reference foil for each metal are also shown.

(Fig. 10d) shows metallic Pd. The same cannot be said for the near edge structure of Cu in the HEA NPs, shown in Fig. 10e, which varied greatly when compared to the reference foil. While the near edge energies and intensities for the two samples are similar, the NP sample lacks the pre-edge feature, typical of 3d transition metals,[57] indicating the presence of Cu oxide in the NPs, in agreement with the XPS results.

Noble-metal HEA NPs have attracted great interest for electrocatalysts due to the high activity they display toward a variety of electrochemical processes, such as CO$_2$ reduction reaction (CO$_2$RR),[9] hydrogen evolution reaction (HER),[17,44,45] and alcohol oxidation reaction.[16] The potential applications of the synthesized AgCuPdPtAu HEA nanoparticles are geared toward their use as electrocatalysts for HER and CO$_2$RR. Of the five noble metals in the HEA nanoparticles, Pt and Pd have demonstrated great catalytic performance for HER.[58,59] It will be interesting to see whether the AuCuPdPtAu HEA nanoparticles provide enhanced HER activity due to the synergistic effect by alloying the five elements, which is currently pursued in our lab. For the application for the electrochemical CO$_2$RR, Au, Ag, and Pd have been identified as promising catalysts to selectively form CO, whereas Pt can be introduced to explore the geometric effect.[60–63] Cu, on the other hand, is known to catalyze the formation of a mixture of C2+ products such as hydrocarbons and oxygenates.[62,63] Tuning the atomic composition in the AuCuPdPtAu HEA nanoparticles to have one metal component rich in particular will allow us to investigate the product distribution in the electrochemical CO$_2$RR and understand the process better.

4. Conclusions

In summary, we have produced the quinary AgCuPdPtAu HEA NPs using the liquid-state dewetting technique of PLiD. This production method is a facile approach applicable to metals of both low (*e.g.*, Au, Ag, and Cu) and high (*e.g.*, Pt and Pd) melting points. The instantaneous heating and rapid cooling in PLiD allow for the successful mixing of different metal atoms, forming the quinary HEA NPs. We have shown that the atomic composition in the HEA NPs can be controlled by varying the thickness of composite metal in the multi-layer thin films prior to dewetting. The electronic structure and the charge redistribution in the produced AgCuPdPtAu HEA NPs were studied by XPS and XANES. The XPS valence band spectra provide strong evidence of randomization of different metal components in the HEA NPs by the significant narrowing in the overall d band and the featureless VB spectra. The XPS core-level spectra and XANES spectra of the composite metals lend further support for the d-charge redistributions among the five metal atoms of Ag, Cu, Pd, Pt, and Au. These results clearly indicate that PLiD is a viable technique for controlled fabrication of HEA NPs and X-ray spectroscopic techniques are powerful in the analysis of these materials. These works open up immense opportunities for future investigation of noble metal HEA NPs, which in turn will provide a testing ground for the advancement of X-ray spectroscopic techniques such as high energy resolution fluorescence detection (HERFD) XAS, valence to core transition, resonant inelastic X-ray scattering (RIXS)/resonant X-ray emission spectroscopy (RXES), among others.

Data availability

The data supporting this article have been included in the main manuscript or as part of the ESI.†

Conflicts of interest

The authors declare no conflicts of interest.

Acknowledgements

References

1 J. W. Yeh, S. K. Chen, S. J. Lin, J. Y. Gan, T. S. Chin, T. T. Shun, C. H. Tsau and S. Y. Chang, *Adv. Eng. Mater.*, 2004, **6**, 299–303.

2 B. Cantor, I. Chang, P. Knight and A. Vincent, *Mater. Sci. Eng., A*, 2004, **375**, 213–218.

3 E. P. George, D. Raabe and R. O. Ritchie, *Nat. Rev. Mater.*, 2019, **4**, 515–534.

4 Y. Yao, Q. Dong, A. Brozena, J. Luo, J. Miao, M. Chi, C. Wang, I. G. Kevrekidis, Z. J. Ren, J. Greeley, G. Wang, A. Anapolsky and L. B. Hu, *Science*, 2022, **376**, eabn3103.

5 Y. Sun and S. Dai, *Sci. Adv.*, 2021, **7**, eabg1600.

6 Y. Xin, S. H. Li, Y. Y. Qian, W. K. Zhu, H. B. Yuan, P. Y. Jiang, R. H. Guo and L. B. Wang, *ACS Catal.*, 2020, **10**, 11280–11306.

7 Y. Yao, Z. Huang, P. Xie, S. D. Lacey, R. J. Jacob, H. Xie, F. Chen, A. Nie, T. Pu and M. Rehwoldt, *Science*, 2018, **359**, 1489–1494.

8 P. Xie, Y. Yao, Z. Huang, Z. Liu, J. Zhang, T. Li, G. Wang, R. Shahbazian-Yassar, L. Hu and C. Wang, *Nat. Commun.*, 2019, **10**, 4011.

9 S. Nellaiappan, N. K. Katiyar, R. Kumar, A. Parui, K. D. Malviya, K. Pradeep, A. K. Singh, S. Sharma, C. S. Tiwary and K. Biswas, *ACS Catal.*, 2020, **10**, 3658–3663.

10 D. Zhang, H. Zhao, X. Wu, Y. Deng, Z. Wang, Y. Han, H. Li, Y. Shi, X. Chen and S. Li, *Adv. Funct. Mater.*, 2021, **31**, 2006939.

11 S. Gao, S. Hao, Z. Huang, Y. Yuan, S. Han, L. Lei, X. Zhang, R. Shahbazian-Yassar and J. Lu, *Nat. Commun.*, 2020, **11**, 2016.

12 H. Li, Y. Han, H. Zhao, W. Qi, D. Zhang, Y. Yu, W. Cai, S. Li, J. Lai and B. Huang, *Nat. Commun.*, 2020, **11**, 5437.

13 X. Y. Sun and Y. G. Sun, *Chem. Soc. Rev.*, 2024, **53**, 4400–4433.

14 J. J. Liang, G. H. Cao, M. Q. Zeng and L. Fu, *Chem. Soc. Rev.*, 2024, **53**, 6021–6041.

15 M. P. Singh and C. Srivastava, *Mater. Lett.*, 2015, **160**, 419–422.

16 D. Wu, K. Kusada, T. Yamamoto, T. Toriyama, S. Matsumura, S. Kawaguchi, Y. Kubota and H. Kitagawa, *J. Am. Chem. Soc.*, 2020, **142**, 13833–13838.

17 M. Liu, Z. Zhang, F. Okejiri, S. Yang, S. Zhou and S. Dai, *Adv. Mater. Interfaces*, 2019, **6**, 1900015.

18 Y. Yang, B. A. Song, X. Ke, F. Y. Xu, K. N. Bozhilov, L. B. Hu, R. Shahbazian-Yassar and M. R. Zachariah, *Langmuir*, 2020, **36**, 1985–1992.

19 H. Y. Qiao, M. T. Saray, X. Z. Wang, S. M. Xu, G. Chen, Z. N. Huang, C. J. Chen, G. Zhong, Q. Dong, M. Hong, H. Xie, R. Shahbazian-Yassar and L. B. Hu, *ACS Nano*, 2021, **15**, 14928–14937.

20 H. Q. Jiang, X. T. Liu, M. N. Zhu, J. Xu, L. C. An, P. F. Sui, J. L. Luo and G. J. Cheng, *Sci. Adv.*, 2022, **8**, eabm6541.

21 R. Rawat, N. P. Blanchard, Y. Shadangi, A. Tripathi and D. Amans, *J. Phys. Chem. C*, 2024, **128**, 19815–19828.

22 J. Bischof, D. Scherer, S. Herminghaus and P. Leiderer, *Phys. Rev. Lett.*, 1996, **77**, 1536–1539.

23 J. Trice, D. Thomas, C. Favazza, R. Sureshkumar and R. Kalyanaraman, *Phys. Rev. B: Condens. Matter Mater. Phys.*, 2007, **75**, 235439.

24 A. J. Fulton, V. O. Kollath, K. Karan and Y. J. Shi, *Nanoscale Adv.*, 2020, **2**, 896–905.

25 D. Gentili, G. Foschi, F. Valle, M. Cavallini and F. Biscarini, *Chem. Soc. Rev.*, 2012, **41**, 4430–4443.

26 H. A. El-Sayed, C. A. Horwood, E. Owusu-Ansah, Y. J. J. Shi and V. I. Birss, *Phys. Chem. Chem. Phys.*, 2015, **17**, 11062–11069.

27 L. Q. Ly, A. J. Fulton, S. N. Bonvicini and Y. J. Shi, *Nanotechnology*, 2021, **32**, 335301.

28 Y. Wu, J. D. Fowlkes, N. A. Roberts, J. A. Diez, L. Kondic, A. G. Gonzalez and P. D. Rack, *Langmuir*, 2011, **27**, 13314–13323.

29 E. Owusu-Ansah, V. I. Birss and Y. J. Shi, *J. Phys. Chem. C*, 2020, **124**, 23387–23393.

30 J. D. Fowlkes, L. Kondic, J. Diez, Y. Y. Wu and P. D. Rack, *Nano Lett.*, 2011, **11**, 2478–2485.

31 Y. Oh, J. Lee and M. Lee, *Appl. Surf. Sci.*, 2018, **434**, 1293–1299.

32 S. N. Bonvicini, A. Hoang, V. I. Birss, S. K. Purdy, R. Sammynaiken, T. K. Sham and Y. J. Shi, *J. Phys. Chem. C*, 2023, **127**, 13945–13957.

33 H. Krishna, N. Shirato, S. Yadavali, R. Sachan, J. Strader and R. Kalyanaraman, *ACS Nano*, 2011, **5**, 470–476.

34 Y. J. Oh, J. H. Kim, C. V. Thompson and C. A. Ross, *Nanoscale*, 2013, **5**, 401–407.

35 D. Spanu, S. Recchia, S. Mohajernia, O. Tomanec, S. Kment, R. Zboril, P. Schmuki and M. Altomare, *ACS Catal.*, 2018, **8**, 5298–5305.

36 S. N. Bonvicini and Y. J. Shi, *ACS Appl. Nano Mater.*, 2022, **5**, 14850–14861.

37 N. Fairley, V. Fernandez, M. Richard-Plouet, C. Guillot-Deudon, J. Walton, E. Smith, D. Flahaut, M. Greiner, M. Biesinger and S. Tougaard, *Appl. Surf. Sci. Adv.*, 2021, **5**, 100112.

38 B. Ravel and M. Newville, *Appl. Surf. Sci. Adv.*, 2021, **5**, 100112.

39 L. Q. Ly, S. N. Bonvicini and Y. J. Shi, *J. Phys. Chem. C*, 2025, **129**, 4553–4564.

40 D. N. Wang, X. Y. Cui, Q. F. Xiao, Y. F. Hu, Z. Q. Wang, Y. M. Yiu and T. K. Sham, *AIP Adv.*, 2018, **8**, 065210.

41 P. N. Duchesne, Z. Y. Li, C. P. Deming, V. Fung, X. J. Zhao, J. Yuan, T. Regier, A. Aldalbahi, Z. Almarhoon, S. W. Chen, D. E. Jiang, N. F. Zheng and P. Zhang, *Nat. Mater.*, 2018, **17**, 1033–1039.

42 T. K. Sham, A. Bzowski, M. Kuhn and C. C. Tyson, *Solid State Commun.*, 1991, **80**, 29–32.

43 A. Bzowski, M. Kuhn, T. K. Sham, J. A. Rodriguez and J. Hrbek, *Phys. Rev. B: Condens. Matter Mater. Phys.*, 1999, **59**, 13379–13393.

44 D. S. Wu, K. Kusada, T. Yamamoto, T. Toriyama, S. Matsumura, I. Gueye, O. Seo, J. Kim, S. Hiroi and O. Sakata, *Chem. Sci.*, 2020, **11**, 12731–12736.

45 D. S. Wu, K. Kusada, Y. Nanba, M. Koyama, T. Yamamoto, T. Toriyama, S. Matsumura, O. Seo, I. Gueye, J. Kim, L. S. R. Kumara, O. Sakata, S. Kawaguchi, Y. Kubota and H. Kitagawa, *J. Am. Chem. Soc.*, 2022, **144**, 3365–3369.

46 M. Tchaplyguine, M. H. Mikkela, C. F. Zhang, T. Andersson and O. Bjorneholm, *J. Phys. Chem. C*, 2015, **119**, 8937–8943.

47 M. Kuhn and T. K. Sham, *Phys. Rev. B: Condens. Matter Mater. Phys.*, 1994, **49**, 1647–1661.

48 C. C. Tyson, A. Bzowski, P. Kristof, M. Kuhn, R. Sammynaiken and T. K. Sham, *Phys. Rev. B: Condens. Matter Mater. Phys.*, 1992, **45**, 8924–8928.

49 R. Belkhou, N. T. Barrett, C. Guillot, M. Fang, A. Barbier, J. Eugene, B. Carriere, D. Naumovic and J. Osterwalder, *Surf. Sci.*, 1993, **297**, 40–56.

50 J. M. Zhang, D. N. Oko, S. Garbarino, R. Imbeault, M. Chaker, A. C. Tavares, D. Guay and D. L. Ma, *J. Phys. Chem. C*, 2012, **116**, 13413–13420.

51 I. Coulthard and T. K. Sham, *Phys. Rev. Lett.*, 1996, **77**, 4824–4827.

52 J. Li, C. H. Liu, M. N. Banis, D. Vaccarello, Z. F. Ding, S. D. Wang and T. K. Sham, *J. Phys. Chem. C*, 2017, **121**, 24861–24870.

53 F. Capece, V. Di Castro, C. Furlani, G. Mattogno, C. Fragale, M. Gargano and M. Rossi, *J. Electron Spectrosc. Relat. Phenom.*, 1982, **27**, 119–128.

54 P. Zhang and T. K. Sham, *Phys. Rev. Lett.*, 2003, **90**, 245502.

55 A. Bzowski, Y. Yiu and T. K. Sham, *Phys. Rev. B: Condens. Matter Mater. Phys.*, 1995, **51**, 9515–9520.

56 M. Kuhn, A. Bzowski and T. K. Sham, *Hyperfine Interact.*, 1994, **94**, 2267–2272.

57 J. Timoshenko and B. R. Cuenya, *Chem. Rev.*, 2020, **121**, 882–961.

58 J. M. van der Zalm, J. Quintal, S. A. Hira, S. Chen and A. Chen, *Electrochim. Acta*, 2023, **439**, 141715.

59 N. Dubouis and A. Grimaud, *Chem. Sci.*, 2019, **10**, 9165–9181.

60 W. L. Zhu, R. Michalsky, Ö. Metin, H. F. Lv, S. J. Guo, C. J. Wright, X. L. Sun, A. A. Peterson and S. H. Sun, *J. Am. Chem. Soc.*, 2013, **135**, 16833–16836.

61 C. Kim, H. S. Jeon, T. Eom, M. S. Jee, H. Kim, C. M. Friend, B. K. Min and Y. J. Hwang, *J. Am. Chem. Soc.*, 2015, **137**, 13844–13850.

62 D. Gao, H. Zhou, F. Cai, J. Wang, G. Wang and X. Bao, *ACS Catal.*, 2018, **8**, 1510–1519.

63 P. Lu, J. Zhou, Y. Hu, J. Yin, Y. Wang, J. Yu, Y. Ma, Z. Zhu, Z. Zeng and Z. Fan, *J. Mater. Chem. A*, 2021, **9**, 19025–19053.